Single-crystal neutron diffraction study of the insulating phase in $NdBaMn_2O_6$

S. Yamada,[1] R. Kiyanagi,[2] A. Nakao,[3] H. Sagayama,[4] and T. Arima[5]

[1]*Department of Materials System Science, Yokohama City University, Yokohama 236-0027, Japan*
[2]*J-PARC Center, Japan Atomic Energy Agency, Tokai, Ibaraki 319-1195, Japan*
[3]*Comprehensive Research Organization for Science and Society (CROSS), Tokai, Ibaraki 319-1106, Japan*
[4]*Nagoya University Synchrotron Radiation Research Center (NUSR), Nagoya University, Nagoya 464-8603, Japan and Graduate School of Engineering, Nagoya University, Nagoya 464-8603, Japan*
[5]*Department of Advanced Materials Science, The University of Tokyo, Kashiwa 277-8561, Japan*

(Received 5 January 2026; revised 11 March 2026; accepted 28 April 2026; published 22 May 2026)

We report a single-crystal neutron diffraction study of the crystal and magnetic structures of $NdBaMn_2O_6$ in its insulating phases, performed on a well-characterized sample that exhibits room-temperature low-field colossal magnetoresistance (CMR). Previous studies have reported conflicting results regarding the crystal structure and the presence or absence of charge-orbital ordering, likely due to differences in sample form and measurement techniques. By using a single crystal in which CMR is directly observed, we clarify these inconsistencies and establish a unified structural picture. This study establishes that the insulating phases correspond to a charge-orbital-ordered state in $NdBaMn_2O_6$. We find that both the paramagnetic and antiferromagnetic insulating phases adopt a $2\sqrt{2}a_p \times \sqrt{2}a_p \times 2c_p$ unit cell with space group $P2_1am$ and exhibit $(3x^2 - r^2)/(3y^2 - r^2)$-type charge and orbital ordering. The antiferromagnetic phase shows an A-type magnetic structure with inequivalent Mn moments arising from this ordering. These results demonstrate that the insulating phases correspond to a charge-orbital-ordered state and suggest that the observed CMR originates from the competition between charge-orbital ordering and magnetic structures. In addition, the polar crystal symmetry implies the presence of spontaneous polarization, mainly arising from oxygen displacements.

DOI: 10.1103/y4sd-sl69

I. INTRODUCTION

The electric and magnetic phase diagrams of double-perovskite manganites, $REBaMn_2O_6$, differ markedly from those of the half-doped manganites, $RE_{0.5}Ba_{0.5}MnO_3$, because of the suppression of cation disorder through the alternate ordering of RE and Ba ions, where RE denotes a trivalent rare-earth element [1–15]. In $NdBaMn_2O_6$, one of these double-perovskite manganites, the metal-insulator transition temperature (T_{MI}) is about 300 K. When a magnetic field exceeding 2 T is applied, T_{MI} decreases with increasing field strength; that is, a room-temperature, low-field colossal magnetoresistance (CMR) has been observed just below T_{MI}[16]. Thus, $NdBaMn_2O_6$ is of considerable interest for both fundamental studies and potential applications.

Previous investigations on polycrystalline samples reported that T_{MI} coincided with the Néel temperature (T_N). However, using single crystals, we demonstrated that the magnetic phase just below T_{MI} is paramagnetic, and that T_N is 235 K [8,17]. Furthermore, synchrotron x-ray diffraction revealed that the insulating phase below T_{MI} exhibits $x^2 - y^2$-type orbital ordering with a $\sqrt{2}a_p \times \sqrt{2}a_p \times c_p$ unit cell [17] (where a_p and c_p are the lattice constants of the tetragonal unit cell, as illustrated in the inset of Fig. 1). This structure is consistent with the layered (A-type) antiferromagnetic order previously reported by powder neutron diffraction but does not fully explain the insulating behavior within the c plane.

More recently, synchrotron x-ray diffraction measurements on large single crystals revealed that the insulating phase adopts a $2\sqrt{2}a_p \times \sqrt{2}a_p \times 2c_p$ unit cell, identical to that of the high-temperature charge-orbital-ordered (HTCOO) phase of $SmBaMn_2O_6$[17,18]. Such charge-orbital ordering can account for the insulating conduction within the c plane. However, it does not explain why the antiferromagnetic phase exhibits an A-type magnetic structure. Very recently, convergent-beam electron diffraction suggested that the insulating phase is not charge-orbital ordered despite its $2\sqrt{2}a_p \times \sqrt{2}a_p \times 2c_p$ unit cell [19]. This study also reported that the space group of the insulating phase is $P2_1am$ (No. 26), a member of the polar point group, implying the presence of spontaneous polarization. Other studies using powder synchrotron x-ray diffraction reported that the space groups below T_N and above T_{MI} are the same as those reported in Ref. [17], whereas the crystal structure in the temperature range $T_N < T < T_{MI}$ is a coexistence of these structures [20,21]. Thus, although numerous studies have reported on the crystal structure of $NdBaMn_2O_6$, the reported results vary depending on the sample form and measurement technique, and a unified understanding has not yet been established. Moreover, the room-temperature, low-field CMR has so far been observed only in millimeter-sized single crystals. Therefore, in order to elucidate the origin of the room-temperature, low-field CMR, it is essential to determine the crystal and magnetic structures using the same single-crystal specimen in which the CMR was previously observed [16].

To this end, we performed single-crystal neutron structure analysis on a $NdBaMn_2O_6$ single crystal that had been

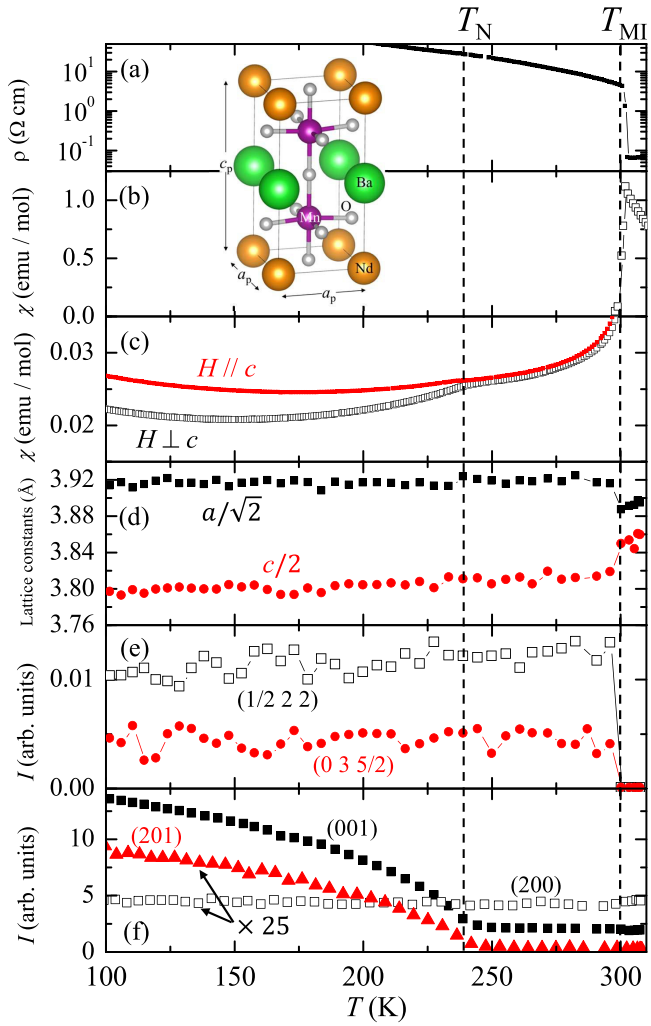

FIG. 1. Temperature dependence of (a) electrical resistivity, (b) magnetic susceptibility, (c) magnetic anisotropy below 300 K, (d) lattice constants, (e) intensities of superlattice reflections, and (f) magnetic reflections in $NdBaMn_2O_6$. The magnetic susceptibility was measured under a magnetic field of 10 kOe. T_{MI} and T_N denote the metal-insulator transition and Néel temperatures, respectively. The inset shows the schematic tetragonal unit cell of $NdBaMn_2O_6$. Lattice constants in panel (d) and reflection indices in panels (e) and (f) are indexed based on the $\sqrt{2}a_p \times \sqrt{2}a_p \times 2c_p$ unit cell.

verified to exhibit CMR and determined the crystal and magnetic structures in the paramagnetic insulating (PI) and antiferromagnetic insulating (AFI) phases. In this paper, we reveal that these insulating phases correspond to a $(3x^2 - r^2)/(3y^2 - r^2)$-type charge- and orbital-ordered state. This result suggests that the CMR originates from the melting of the charge-ordered state, which is consistent with the sharp change in electrical resistivity induced by an external magnetic field [22,23]. To the best of our knowledge, few previous studies explicitly identified these insulating phases as a charge-ordered state. These findings imply that the stability of the charge- and orbital-ordered state in the insulating phases of $NdBaMn_2O_6$ may depend sensitively on the sample size and quality, and such instability may be responsible for the melting of the ordered state under a low magnetic field, leading to CMR.

II. METHODS

A single crystal of $NdBaMn_2O_6$ used in this study was identical to that employed in our previous work [16]. Magnetization measurements were performed using a commercial superconducting quantum interference device (SQUID) magnetometer (Quantum Design MPMS-XL). Electrical resistivity was measured by the conventional four-probe method. Neutron diffraction experiments were conducted on the time-of-flight single-crystal neutron diffractometer, SENJU, at the Materials and Life Science Experimental Facility (MLF) [24].

The measured data were first processed using STARGazer, the standard software for SENJU [25]. The integrated intensities obtained from STARGazer were subsequently analyzed using JANA, a software package capable of refining both crystal and magnetic structures [26]. The diffraction data were indexed using an expanded $2\sqrt{2}a_p \times 2\sqrt{2}a_p \times 2c_p$ unit cell in order to properly read and handle the reflections appearing at half-integer positions originating from a twin domain, so that they can be incorporated into the refinement described later. In the structural refinement, atoms were initially placed in a $2\sqrt{2}a_p \times \sqrt{2}a_p \times 2c_p$ unit cell with space group $P2_1am$. The expanded unit cell corresponds to the supercell that was constructed by adding translational symmetry along the b axis, namely (0, 1/2, 0) to the original cell. This preserves $P2_1am$ symmetry of the true unit cell while readily accommodating the 90° twin domain into the refinement. Note that the possibility of the doubling of both the a and b axis, that is $2\sqrt{2}a_p \times 2\sqrt{2}a_p \times 2c_p$ cell as a true unit cell, was eliminated because of the absence of $(h + 1/2, k + 1/2, l)$ type reflections (see Fig. S1 in the Supplemental Material [27]).

The magnetic structure of the antiferromagnetic insulating phase was analyzed using the magnetic form factor of Mn^{3+}. Essentially, the same results were obtained when the Mn^{4+} form factor was used. Initially, all three components of the Mn magnetic moments were refined. The a- and c-axis components were found to be smaller than 0.2 μ_B with comparable uncertainties, therefore, only the b-axis components were refined, with the a- and c-axis components fixed to zero. The resulting b-axis magnetic moment was consistent between the two refinement models within the margin of uncertainty.

The valence state of each Mn ion was estimated using the bond-valence-sum (BVS) method [28,29]. The valence V_{BVS} was calculated as

$$V_{BVS} = \sum_i \exp\left[\frac{d_0 - d_i}{B}\right], \tag{1}$$

where d_i is the distance between the Mn ion and ith coordinating oxygen atom. The empirical parameter B was set to 0.37 Å and d_0 was taken as 1.732 Å for Mn^{3+} and 1.750 Å for Mn^{4+}. The $3d$-orbital shapes were determined using Kanamori's representation combined with normal-mode analysis [30,31].

III. RESULTS AND DISCUSSION

Figure 1 shows the temperature dependence of (a) electrical resistivity, (b) magnetic susceptibility, (c) magnetic

TABLE I. Refined structural parameters for $NdBaMn_2O_6$ at 270 K with space group $P2_1am$ (No. 26) and orthorhombic symmetry. The R factors are $R = 6.03\%$ and $R_w = 6.69\%$. Lattice parameters are $a = 11.087(5)$ Å, $b = 5.544(5)$ Å, $c = 15.273(8)$ Å. Goodness-of-fit indicator S (all reflections) is 2.54. The symbol of V_{BVS} denotes the Mn-ion valences estimated by the bond-valence-sum method. Q_2 and Q_3 represent the distortion modes of the MnO_6 octahedra.

	Occupancy	Site	x	y	z	B_{iso}(Å^2)	V_{BVS}	Q_2(Å)	Q_3(Å)
Nd1	1	2*a*	0.0062(3)	0.5042(4)	0	0.0054(6)			
Nd2	1	2*b*	0.0049(3)	0.5058(4)	0.5	0.0029(5)			
Nd3	1	2*a*	0.2491(4)	0.0034(6)	0	0.0056(8)			
Nd4	1	2*b*	0.2489(4)	0.0046(8)	0.5	0.0084(10)			
Ba1	1	4*c*	0.0037(3)	0.5038(6)	0.2534(3)	0.0047(4)			
Ba2	1	4*c*	0.2522(3)	0.9966(6)	0.2517(5)	0.0036(4)			
Mn1	1	4*c*	0.0043(5)	0.0021(3)	0.1257(3)	0.0031(6)	3.14(4)	±0.072(6)	−0.079(6)
Mn2	1	4*c*	0.0045(6)	0.0102(4)	0.6235(4)	0.0037(6)	3.78(5)	±0.032(6)	−0.026(7)
Mn3	1	4*c*	0.2539(5)	0.4956(8)	0.1210(4)	0.0023(6)	3.72(6)	±0.008(7)	−0.028(7)
Mn4	1	4*c*	0.2544(5)	0.4938(8)	0.6226(4)	0.0020(6)	3.15(5)	±0.184(6)	−0.102(7)
O1	1	2*a*	0.0091(5)	0.0036(8)	0	0.0157(7)			
O2	1	2*b*	0.0235(2)	0.0537(4)	0.5	0.0000(2)			
O3	1	2*a*	0.2311(4)	0.4922(8)	0	0.0128(9)			
O4	1	2*b*	0.2305(4)	0.4892(8)	0.5	0.0097(7)			
O5	1	4*c*	0.9929(2)	0.0014(4)	0.2516(3)	0.0040(2)			
O6	1	4*c*	0.2567(3)	0.5016(6)	0.2496(4)	0.0089(3)			
O7	1	4*c*	0.1271(4)	0.2480(8)	0.12013(19)	0.0116(6)			
O8	1	4*c*	0.1252(3)	0.2636(4)	0.62604(16)	0.0032(3)			
O9	1	4*c*	0.3758(3)	0.2460(8)	0.1089(3)	0.0138(7)			
O10	1	4*c*	0.3830(2)	0.2234(4)	0.60508(17)	0.0042(3)			
O11	1	4*c*	0.1316(4)	0.7446(8)	0.1168(2)	0.0140(6)			
O12	1	4*c*	0.1222(2)	0.7692(6)	0.61458(16)	0.0051(4)			
O13	1	4*c*	0.3739(3)	0.7372(8)	0.1071(3)	0.0142(7)			
O14	1	4*c*	0.3758(2)	0.7360(4)	0.6097(2)	0.0010(3)			

anisotropy below 300K, (d) lattice constants, (e) intensities of superlattice reflections, and (f)magnetic reflections. The inset illustrates the tetragonal unit cell of $NdBaMn_2O_6$. The lattice constants in Fig. 1(d) and the reflection indices in Figs. 1(e) and (f) are given for the $\sqrt{2}a_p \times \sqrt{2}a_p \times 2c_p$ unit cell. Below $T_{MI} = 300$ K, the resistivity increases by nearly two orders of magnitude, while the magnetization decreases abruptly. Anisotropic magnetization develops below $T_N = 235$ K. Sharp changes in the a- and the c-axis lattice constants are also observed at T_{MI} [Fig. 1(d)].

These behaviors near T_{MI} and T_N are consistent with our previous reports [17]. The lattice constants and their temperature dependences differ slightly from those obtained by synchrotron x-ray diffraction, owing to differences in instrumental resolution of neutron and synchrotron measurements. The appearance of superlattice reflections associated with twofold periodicity along the a and c axes below T_{MI} [Fig. 1(e)] indicates that the unit cell below T_{MI} is $2\sqrt{2}a_p \times \sqrt{2}a_p \times 2c_p$, consistent with earlier studies [16,19]. Reciprocal-space maps on $l = 0$ at 310 K ($T_{MI} < T$) and 270 K ($T_N < T < T_{MI}$) are provided in Figs. S1 and S2 of the Supplemental Material [27].

The superlattice reflection intensities in Fig. 1(e) remain essentially unchanged below T_N, whereas magnetic reflections emerge [Fig. 1(f)]. Notably, reflections at $(h + 1/2, k + 1/2, l)$ and $(h + 1/2, k + 1/2, l + 1/2)$ are absent (see Figs. S3 and S4 in the Supplemental Material [27]), indicating that the magnetic structure below T_N is not of the CE-type, which is frequently seen in half-doped perovskite manganites (e.g., $Nd_{0.5}Sr_{0.5}MnO_3$ and $Pr_{0.5}Ca_{0.5}MnO_3$) [32] and in double-perovskite manganites (e.g., $SmBaMn_2O_6$ and $YBaMn_2O_6$) [9,15,33]. In contrast, the reflection intensities of (001) and (201) increase gradually with decreasing temperature below T_N, whereas the intensity of the (200) reflection remains nearly constant [Fig. 1(f)]. These results strongly suggest an A-type (layered) antiferromagnetic structure with a finite magnetic component perpendicular to the c axis, consistent with previous powder neutron diffraction results [8]. The detailed magnetic structure of the AFI phase, determined from the single-crystal diffraction data, is described below.

Tables I and II summarize the refined structure parameters at 270 K ($T_N < T < T_{MI}$) and 100 K ($T < T_N$) corresponding to the paramagnetic insulating (PI) and antiferromagnetic insulating (AFI) phases, respectively. Both phases adopt the same $2\sqrt{2}a_p \times \sqrt{2}a_p \times 2c_p$ unit cell with space group $P2_1am$ (No. 26). This structure contains four crystallographically independent Mn sites, labeled Mn1-Mn4. The four MnO_2 layers in the $2\sqrt{2}a_p \times \sqrt{2}a_p \times 2c_p$ unit cell are divided into two types according to the Mn sites, layers composed of Mn1 and Mn3 are denoted $MnO_2 - \alpha$, whereas those composed of Mn2 and Mn4 are denoted $MnO_2 - \beta$.

Previous studies using powder synchrotron x-ray diffraction reported a coexistence of the $P2_1am$ and $Cmmm$ structures in the temperature range of $220 - 280$ K [20,21]. This temperature range approximately corresponds to the PI phase identified in the present study. As shown in Fig. S5 of the Supplemental Material [27], the (040) reflection remains a single peak with no splitting or shoulder formation throughout

TABLE II. Refined structural and magnetic parameters for $NdBaMn_2O_6$ at 100 K with magnetic space group $P2_1am$ (No. 26.1.168) and orthorhombic symmetry. The R factors are $R = 5.34\%$ and $R_w = 5.83\%$. Lattice parameters are $a = 11.060(3)$ Å, $b = 5.530(3)$ Å, $c = 15.177(6)$ Å. Goodness-of-fit indicator S (all reflections) is 2.21.V_{BVS} denotes the Mn-ion valences estimated by the bond-valence-sum method. Q_2 and Q_3 indicate the MnO_6 octahedral distortion modes. m represents the magnetic moments along the b axis.

	Occupancy	Site	x	y	z	B_{iso}(Å^2)	V_{BVS}	Q_2(Å)	Q_3(Å)	m (μ_B)
Nd1	1	2*a*	0.0053(3)	0.49940(24)	0	0.0020(4)				
Nd2	1	2*b*	0.0067(3)	0.50140(24)	0.5	0.0016(4)				
Nd3	1	2*a*	0.2486(3)	0.9974(4)	0	0.0035(6)				
Nd4	1	2*b*	0.2475(2)	0.00688(36)	0.5	0.0010(5)				
Ba1	1	4*c*	0.0035(3)	0.50498(26)	0.2509(4)	0.0008(3)				
Ba2	1	4*c*	0.2519(3)	0.0020(4)	0.2513(4)	0.0025(4)				
Mn1	1	4*c*	0.0013(3)	0.00166(24)	0.1262(3)	0.0011(4)	3.20(3)	±0.075(4)	−0.091(5)	3.3(10)
Mn2	1	4*c*	0.0016(3)	0.00802(30)	0.6229(3)	0.0018(4)	3.81(4)	±0.023(3)	−0.039(5)	2.5(12)
Mn3	1	4*c*	0.2507(3)	0.5032(4)	0.1223(3)	0.0013(4)	3.80(4)	±0.006(4)	−0.044(6)	2.9(12)
Mn4	1	4*c*	0.2518(3)	0.4992(4)	0.6216(3)	0.0017(4)	3.25(3)	±0.171(3)	−0.095(6)	2.9(10)
O1	1	2*a*	0.0196(3)	0.0014(4)	0	0.0079(5)				
O2	1	2*b*	0.02195(15)	0.04756(30)	0.5	0.0000(2)				
O3	1	2*a*	0.2319(4)	0.5202(8)	0	0.0170(6)				
O4	1	2*b*	0.2335(3)	0.4798(4)	0.5	0.0029(3)				
O5	1	4*c*	0.9925(2)	0.00180(24)	0.2512(3)	0.0032(3)				
O6	1	4*c*	0.2587(2)	0.50272(36)	0.2487(4)	0.0046(3)				
O7	1	4*c*	0.1291(3)	0.2600(4)	0.1193(2)	0.0086(3)				
O8	1	4*c*	0.12513(19)	0.26284(32)	0.62457(14)	0.0019(2)				
O9	1	4*c*	0.3721(3)	0.2604(4)	0.1078(3)	0.0081(4)				
O10	1	4*c*	0.38259(15)	0.22896(32)	0.60545(16)	0.00195(19)				
O11	1	4*c*	0.1248(3)	0.7522(4)	0.12165(17)	0.0074(4)				
O12	1	4*c*	0.12252(16)	0.76976(32)	0.61495(18)	0.0026(2)				
O13	1	4*c*	0.3762(2)	0.7492(4)	0.1076(3)	0.0082(4)				
O14	1	4*c*	0.37475(15)	0.73702(32)	0.6089(2)	0.0011(2)				

the PI temperature range, and its full width at half maximum is unchanged within experimental uncertainty. Similar single-peak behavior was confirmed for other measured reflections as well. These observations indicate that no peak-profile features suggestive of phase coexistence are present below T_{MI} in our single-crystal samples. This discrepancy may originate from differences in sample characteristics, particularly sample size, as the previous studies were conducted on polycrystalline samples, whereas the present study uses large single crystals. In our samples, both magnetization and

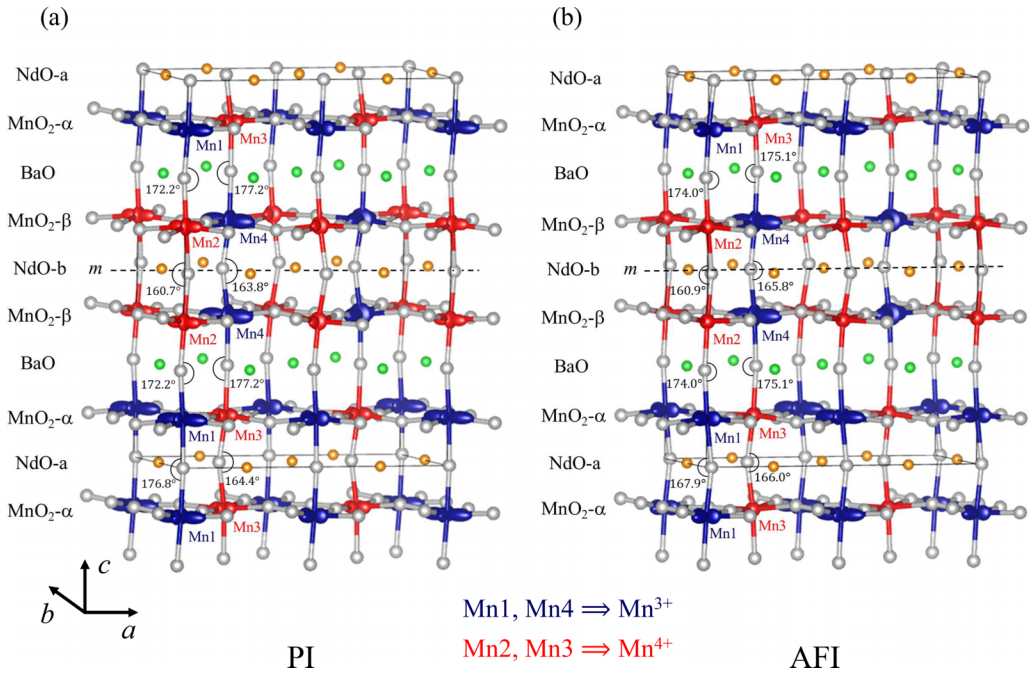

FIG. 2. Crystal structures of (a) the paramagnetic insulating (PI) and (b) the antiferromagnetic insulating (AFI) phases of $NdBaMn_2O_6$.

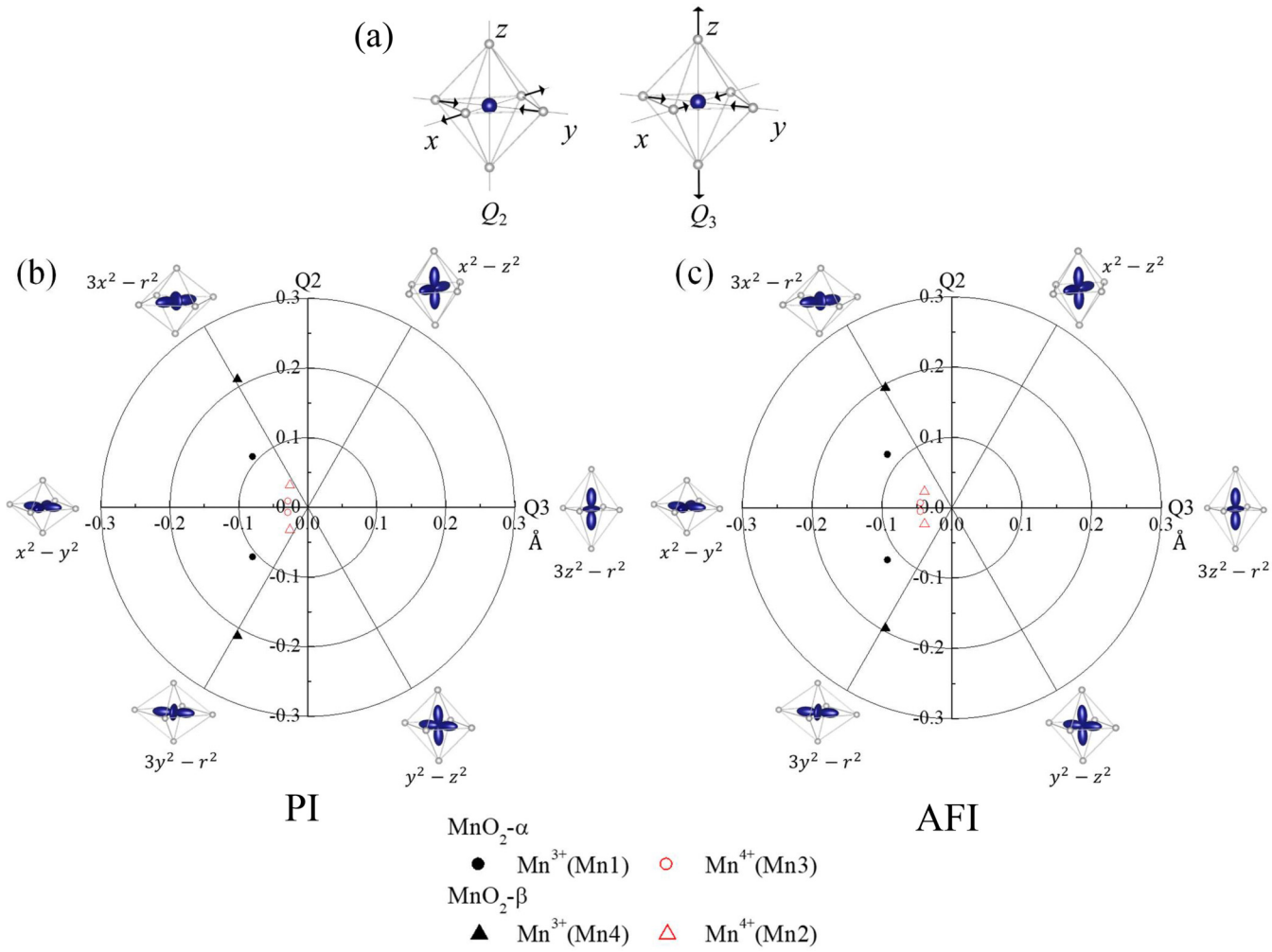

FIG. 3. (a) Schematic representations of the Q_2 and Q_3 distortion modes that directly couple with orbital occupations in the doubly degenerate e_g states. $Q_2 - Q_3$-mode analysis of the MnO_6 octahedra in $NdBaMn_2O_6$ for (b) the PI and (c) AFI the phases. The stabilized orbitals are illustrated for each distorted octahedron.

electrical resistivity exhibit sharp changes at T_{MI}, whereas in previous reports their temperature dependences are much more gradual. A dependence of the temperature evolution of magnetization on sample size has also been reported in $SmBaMn_2O_6$[34].

Bond-valence-sum (BVS) analysis yields valences of approximately +3.2 for Mn1 and Mn4, and +3.8 for Mn2 and Mn3 in both phases. These results clearly indicate charge ordering, in contrast to the convergent-beam electron diffraction study [19]. The charge arrangements of both the PI and AFI phases (Fig. 2) are essentially identical to that of the high-temperature charge-orbital-ordered (HTCOO) phase of $SmBaMn_2O_6$[18], whose magnetic state is paramagnetic. Although the AFI phase of $SmBaMn_2O_6$ shows a distinct charge arrangement from its HTCOO phase, the AFI phase of $NdBaMn_2O_6$ retains the same charge ordering as the PI phase.

The e_g orbital configurations of the Mn ions in the PI phase and the AFI phase were estimated from the Q_2 and Q_3 distortion modes of the MnO_6 octahedra (Fig. 3) [30,31]. In both phases, the orbitals at the Mn1 site are nearly pure the $3x^2 - r^2$ or $3y^2 - r^2$, whereas those at Mn4 sites are slightly hybridized with $y^2 - z^2$ and $x^2 - z^2$, respectively. The estimated e_g orbitals at Mn4 sites are as follows:

(i) for the PI phase: $0.99|3x^2 - r^2\rangle + 0.15|y^2 - z^2\rangle$ or $0.99|3y^2 - r^2\rangle + 0.15|x^2 - z^2\rangle$;

(ii) for the AFI phase: $0.98|3x^2 - r^2\rangle + 0.18|y^2 - z^2\rangle$ or $0.98|3y^2 - r^2\rangle + 0.18|x^2 - z^2\rangle$.

These results indicate slightly stronger orbital hybridization in the AFI phase than in the PI phase.

The detailed magnetic structure of the AFI phase was investigated based on symmetry considerations. Among all the symmetrically allowed models, the A-type antiferromagnetic configuration with the magnetic easy axis aligned along the b axis provided the best agreement with the observed data. This model is fully consistent with the previous discussion based on the behavior of the magnetic reflections [Fig. 1(f)]. Schematic illustrations of the arrangements of the magnetic moments in (a) the $MnO_2 - \alpha$ layer, (b) the $MnO_2 - \beta$ layer, and (c) the a-plane projection are shown in Fig. 4. The magnetic moments of the Mn^{3+} ions are larger than those of Mn^{4+} within the same MnO_2 layers, consistent

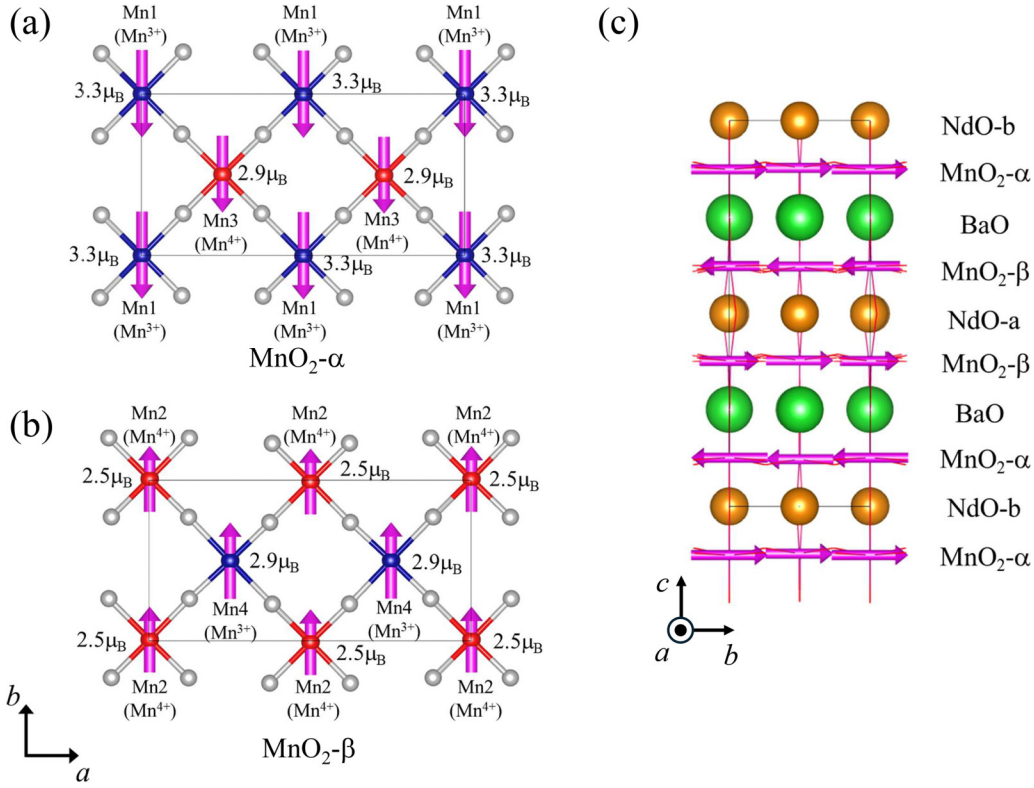

FIG. 4. Schematic representations of the magnetic moment arrangements of the Mn $3d$ electrons in (a) the $MnO_2 - \alpha$ layer, (b) the $MnO_2 - \beta$ layer, and (c) the a-plane projection of the AFI phase.

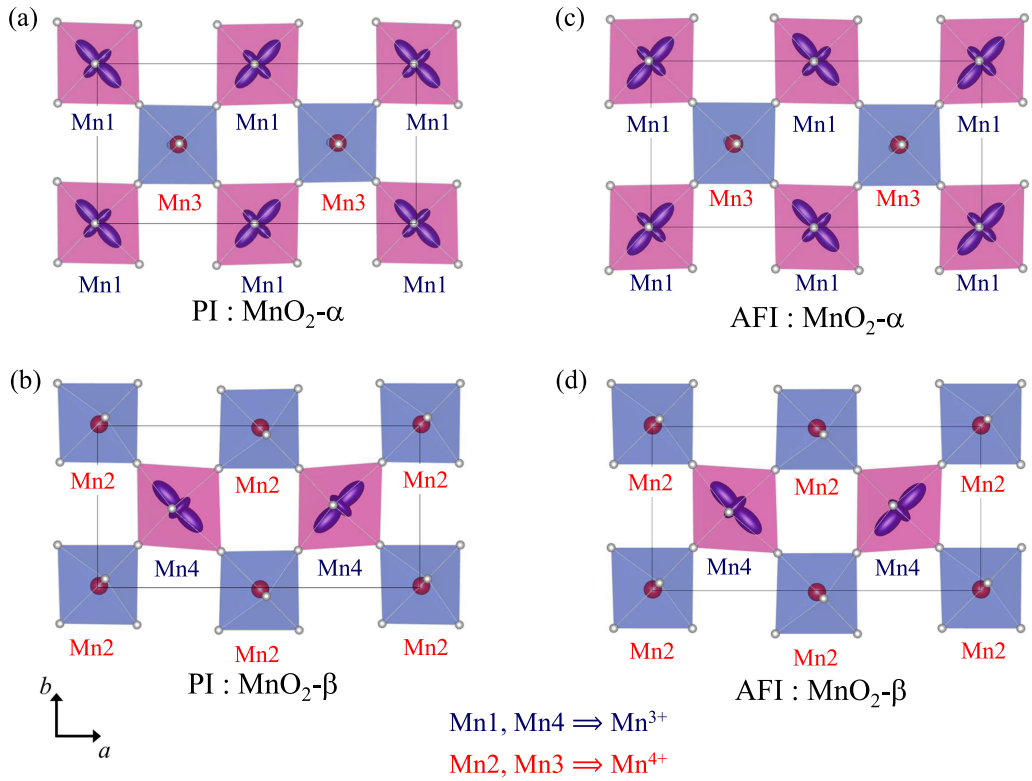

FIG. 5. Schematic illustrations of orbital-ordering patterns in (a), (b) the PI and (c), (d) the AFI phases. Panels (a), (c) and (b), (d) correspond to the $MnO_2 - \alpha$ and $MnO_2 - \beta$ layers, respectively.

TABLE III. The estimated polarizations (μCcm^{-2}) along a axis. "Total," "O," "NdO," and "Charges" denote the total polarization, the contribution from oxygen displacements, the distorion within the NdO layer, and the contribution from Mn-ion charge separation, respectively.

T (K)	Total	O	NdO	Charges
270	4.74	5.05	−0.30	<0.01
100	1.37	1.28	0.10	−0.01

with the higher number of 3d electrons on Mn^{3+}. The ordered moments in $MnO_2-\beta$ layer are smaller than those in the $MnO_2-\alpha$ layers. In general, in perovskite manganites, the $(3x^2-r^2)/(3y^2-r^2)$- and the x^2-y^2-type orbital orderings correspond to CE- and A-type antiferromagnetic structures, respectively [32,35–39]. In the $MnO_2-\alpha$ layer, the e_g orbitals at Mn1 sites exhibit slight hybridization with y^2-z^2 or x^2-z^2, which favors the A-type ordering. Meanwhile, in the $MnO_2-\beta$ layer, the e_g orbitals at Mn4 sites are nearly pure $3x^2-r^2$ or $3y^2-r^2$, which should favor the CE-type ordering. This stronger competition between the observed A-type and the favored CE-type ordering in $MnO_2-\beta$ may render the magnetic structure of $MnO_2-\beta$ less stable, as reflected in its smaller ordered moments. However, the neutron diffraction alone cannot fully explain why the A-type antiferromagnetic structure is stabilized within a $(3x^2-r^2)/(3y^2-r^2)$-type orbital ordering. Recently, Streltsov *et al*. showed via numerical simulations that the ground state of the low temperature phase of $PrBaMn_2O_6$ contains two competing antiferromagnetic structures (A type and CE type) with nearly degenerate energies [40]. A similar energy calculation for $NdBaMn_2O_6$ could help clarify the origin of the coexistence of the A-type antiferromagnetic and the $(3x^2-r^2)/(3y^2-r^2)$-type charge-orbital ordering.

Both the PI and AFI phases can possess spontaneous polarization along the a direction, because both phases belong to the polar point group ($2mm$). Although the orbital-ordering patterns in the insulating phases are similar to those of the high-temperature charge-orbital-ordered (HTCOO) phase of $SmBaMn_2O_6$, the orientations of the extended orbitals differ by 90° between the PI and AFI phase (Fig. 5). These orbital-ordering patterns coincide after a 180° rotation about the b axis or a 180° rotation about the c axis followed by a translation of $0.5a$ along the a axis, indicating that the orbital-ordering configuration correlates with the sign of the spontaneous polarization along the a axis. Table III lists the calculated spontaneous polarizations along the a axis using a point-charge approximation with $Mn^{3.8+}$ and $Mn^{3.2+}$ valences. The analysis indicates that the primary contribution to the polarization originates not from the charge separation between Mn-ions but from the displacement of O^{2-} ions from their ideal positions within the MnO_6 octahedra. The polarization in the AFI phase is smaller than that in the PI phase. This reduction arises mainly from the Mn1–O1–Mn1 bond angle (Fig. 2), which decreases from 176.8° in the PI phase to 167.9° in the AFI phase. Figure 6 shows that the displacements of O^{2-} ions in the BaO and NdO-b layers of

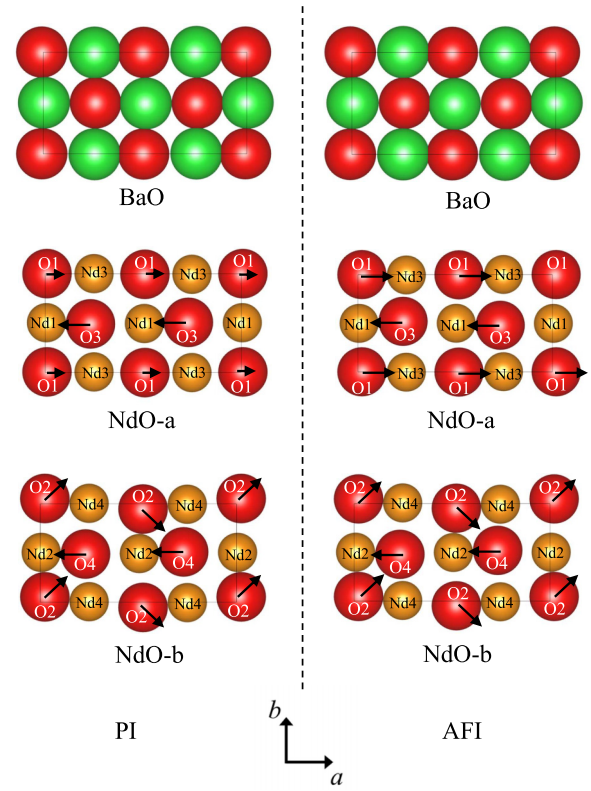

FIG. 6. Schematic representations of BaO, NdO-a, and NdO-b layers in the PI and AFI phases. Arrows indicate the ionic displacements from the ideal double-perovskite structure.

the AFI phase are similar to those in the PI phase. In contrast, the O^{2-} ions at the O1 sites in the NdO-a layer are only weakly distorted in the PI phase, whereas in the AFI phase they distort in the opposite direction to that of the O^{2-} ions at O3 sites. The polarization induced by the distortions of the O^{2-} ions at the O3 sites thus partially cancels that arising from the distortions of the O^{2-} ions at the O1 sites. As a result, the structural modification accompanying the magnetic transition modulates the spontaneous polarization. However, it is also possible that the magnetic and structural transitions coincide accidentally. Therefore, based solely on the present results, no definitive conclusion can be drawn regarding the coupling between magnetic and ferroelectric properties. Further investigations, such as structural analysis under an applied magnetic field, would be necessary to clarify this issue. Moreover, while direct electrical measurement of the polarization is difficult because of the relatively low resistivity (10–100 Ω · cm) of the insulating phases, it may be accessible through optical probes such as second-harmonic generation, as previously observed in the low-temperature charge-orbital-ordered (LTCOO) phase of $SmBaMn_2O_6(P2_1am)$ [41].

IV. CONCLUSION

In summary, our single-crystal neutron diffraction study of $NdBaMn_2O_6$ demonstrates that the insulating phase below T_{MI} exhibits well-defined charge and orbital ordering. The ordering pattern closely resembles that of the high-temperature

charge-orbital-ordered (HTCOO) phase of $SmBaMn_2O_6$. Although the charge and orbital ordering in the antiferromagnetic phase is essentially the same as in the paramagnetic phase, the magnetic structure of the antiferromagnetic phase is not the CE-type but rather an A-type structure, with the magnetic easy axis along the *b* direction. The competition between the charge-orbital-ordering pattern and the magnetic structure may underlie the origin of the room-temperature, low-field colossal magnetoresistance. The space group of the insulating phase is $P2_1am$, indicating a spontaneous polarization along the *a* axis. The estimated spontaneous polarization of the antiferromagnetic phase is smaller than that of the paramagnetic insulating phase.

ACKNOWLEDGMENTS

This study was partly supported by JSPS KAKENHI Grants No. 18K03546 and No. 25K07208. Crystal structures were drawn using the program VESTA [42]. Neutron diffraction measurements were performed using SENJU at the Materials and Life Science Experimental Facility(MLF) of J-PARC under Projects No. 2018B0174 and No. 2023A0054.

DATA AVAILABILITY

The data that support the findings of this article are not publicly available. The data are available from the authors upon reasonable request.

[1] F. Millange, V. Caignaert, B. Domengès, B. Raveau, and E. Suard, Order–disorder phenomena in new $LaBaMn_2O_{6-x}$ CMR Perovskites. Crystal and magnetic structure, Chem. Mater. **10**, 1974 (1998).

[2] V. Caignaert, F. Millange, B. Domengès, B. Raveau, and E. Suard, A new ordered oxygen-deficient manganite Perovskite: $LaBaMn_2O_{5.5}$ crystal and magnetic structure, Chem. Mater. **11**, 930 (1999).

[3] S. V. Trukhanov, I. O. Troyanchuk, M. Hervieu, H. Szymczak, and K. Bärner, Magnetic and electrical properties of $LBaMn_2O_{6-\gamma}$ (L = Pr, Nd, Sm, Eu, Gd, Tb) manganites, Phys. Rev. B **66**, 184424 (2002).

[4] I. O. Troyanchuk, S. V. Trukhaov, M. Hervieu, and G. Szymezak, New family of $LnBaMn_2O_{6-\gamma}$ manganites (Ln = Nd, Sm, and Gd), Crystallogr. Rep. **47**, 658 (2002).

[5] T. Nakajima, H. Kageyama, and Y. Ueda, Successive phase transitions in a metal-ordered manganite Perovskite $YBaMn_2O_6$, J. Phys. Chem. Solids **63**, 913 (2002).

[6] Anthony J. Williams and J. P. Attfield, Alternative charge-order polymorph for half-doped manganites in $TbBaMn_2O_6$, Phys. Rev. B **66**, 220405(R) (2002).

[7] T. Arima, D. Akahoshi, K. Oikawa, T. Kamiyama, M. Uchida, Y. Matsui, and Y. Tokura, Change in charge and orbital alignment upon antiferromagnetic transition in the *A*-site-ordered Perovskite manganese oxide $RBaMn_2O_6$ (R = Tb and Sm), Phys. Rev. B **66**, 140408(R) (2002).

[8] T. Nakajima, H. Kageyama, H. Yoshizawa, K. Ohoyama, and Y. Ueda, Ground state properties of the *A*-site ordered manganites, $RBaMn_2O_6$, J. Phys. Soc. Jpn. **72**, 3237 (2003).

[9] H. Kageyama, T. Nakajima, M. Ichihara, Y. Ueda, H. Yoshizawa, and K. Ohoyama, New stacking variations of the charge and orbital ordering in the metal-ordered manganite $YBaMn_2O_6$, J. Phys. Soc. Jpn. **72**, 241 (2003).

[10] D. Akahoshi, M. Uchida, Y. Tomioka, T. Arima, Y. Matsui, and Y. Tokura, Random potential effect near the bicritical region in Perovskite manganites as revealed by comparison with the ordered Perovskite analogs, Phys. Rev. Lett. **90**, 177203 (2003).

[11] T. Nakajima, H. Yoshizawa, and Y. Ueda, *A*-state randomness effect on structural and physical properties of Ba-based Perovskite manganites, J. Phys. Soc. Jpn. **73**, 2283 (2004).

[12] T. Nakajima, H. Kageyama, M. Ichihara, K. Ohoyama, H. Yoshizawa, and Y. Ueda, Anomalous octahedral distortion and multiple phase transitions in the metal-ordered manganite $YBaMn_2O_6$, J. Solid State Chem. **177**, 987 (2004).

[13] D. Akahoshi, Y. Okimoto, M. Kubota, R. Kumai, T. Arima, Y. Tomioka, and Y. Tokura, Charge-orbital ordering near the multicritical point in *A*-site ordered Perovskites $SmBaMn_2O_6$, Phys. Rev. B **70**, 064418 (2004).

[14] T. Nakajima and Y. Ueda, 1000% colossal magnetoresistance at room temperature in the *A*-site ordered Perovskite manganites $Sm_{1-x}La_{x+y}Ba_{1-y}Mn_2O_6$, J. Appl. Phys. **98**, 046108 (2005).

[15] T. Nakajima, A-site order/disorder effect and room temperature Colossal magnetoresistance in Perovskite manganite, Ph.D. thesis, The University of Tokyo, Tokyo, Japan, 2006.

[16] S. Yamada, N. Abe, H. Sagayama, K. Ogawa, Y. Yamagami, and T. Arima, Room-temperature low-field colossal magnetoresistance in double-Perovskite manganite, Phys. Rev. Lett. **123**, 126602 (2019).

[17] S. Yamada, H. Sagayama, K. Higuchi, T. Sasaki, K. Sugimoto, and T. Arima, Physical properties and crystal structure analysis of double-Perovskite $NdBaMn_2O_6$ by using single crystals, Phys. Rev. B **95**, 035101 (2017).

[18] H. Sagayama, S. Toyoda, K. Sugimoto, Y. Maeda, S. Yamada, and T. Arima, Ferroelectricity driven by charge ordering in the *A*-site ordered Perovskite manganite $SmBaMn_2O_6$, Phys. Rev. B **90**, 241113(R) (2014).

[19] M. S. Islam, D. Morikawa, S. Yamada, B. Aryal, K. Tsuda, and M. Terauchi, Space group determination and first-principles structure optimization of the *A*-site ordered Perovskite-type manganite $NdBaMn_2O_6$, Phys. Rev. B **105**, 174114 (2022).

[20] A. Khatun, P. Aich, A. Schoekel, A. Gloskovskii, S. Panda, N. Mohapatra, S. D. Mahanti, U. Manju, and D. Topwal, Intertwined crystal structure, magnetic, and charge transport properties in mixed valent A-site ordered manganite $NdBaMn_2O_6$, J. Alloys Compd. **988**, 174205 (2024).

[21] J. Blasco, G. Subías, M. L. Sanjuán, J. L. García-Muñoz, F. Fauth, and J. García, Structure and phase transitions in A-site ordered $RBaMn_2O_6$ (R = Pr, Nd) Perovskites with a polar ground state, Phys. Rev. B **103**, 064105 (2021).

[22] Y. Tomioka, A. Asamitsu, H. Kuwahara, Y. Moritomo, and Y. Tokura, Anomalous magnetotransport properties of $Pr_{1-x}Ca_xMnO_3$, J. Phys. Soc. Jpn. **64**, 3626 (1995).

[23] Y. Tomioka, A. Asamitsu, H. Kuwahara, Y. Moritomo, and Y. Tokura, Magnetic-field-induced metal-insulator phenomena in $Pr_{1-x}Ca_xMnO_3$, Phys. Rev. B **53**, R1689(R) (1996).

[24] T. Ohhara, R. Kiyanagi, K. Oikawa, K. Kaneko, T. Kawasaki, I. Tamura, A. Nakao, T. Hanashima, K. Munakata, T. Moyoshi, T. Kuroda, H. Kimura, T. Sakakura, C. Lee, M. Takahashi, K. Ohshima, T. Kiyotani, Y. Noda, and M. Arai, SENJU: A new time-of-flight single-crystal neutron diffractometer at, J-PARC, J. Appl. Crystallogr. **49**, 120 (2016).

[25] T. Ohhara, K. Kusaka, T. Hosoya, K. Kurihara, K. Tomoyori, N. Niimura, I. Tanaka, J. Suzuki, T. Nakatani, T. Otomo, S. Matsuoka, K. Tomita, Y. Nishimaki, T. Ajima, and S. Ryufuku, Development of data processing software for a new TOF single crystal neutron diffractometer at J-PARC, Nucl. Instrum. Methods Phys. Res. Sect. A **600**, 195 (2009).

[26] V. Petricek, M. Dusek, and L. Palatinus, Crystallographic computing system JANA2006: General features, Z. Kristallogr. **229**, 345 (2014).

[27] See Supplemental Material at http://link.aps.org/supplemental/10.1103/y4sd-sl69 for experimental details and additional data.

[28] I. D. Brown and D. Altermatt, Bond-valence parameters obtained from a systematic analysis of the Inorganic Crystal Structure Database, Acta Cryst. **41**, 244 (1985).

[29] W. Liu and H. H. Thorp, Bond valence sum analysis of metal-ligand bond lengths in metalloenzymes and model complexes. 2. Refined distances and other enzymes, Inorg. Chem. **32**, 4102 (1993).

[30] J. Kanamori, Crystal distortion in magnetic compounds, J. Appl. Phys. **31**, S14 (1960).

[31] D. Okuyama, Y. Tokunaga, R. Kumai, Y. Taguchi, T. Arima, and Y. Tokura, and Y. Tomioka, Lattice-form-dependent orbital shape and charge disproportionation in charge- and orbital-ordered manganites, Phys. Rev. B **80**, 064402 (2009).

[32] Y. Tokura and Y. Tomioka, Colossal magnetoresistive manganites, J. Magn. Magn. Mater. **200**, 1 (1999).

[33] R. Kiyanagi, S. Yamada, H. Aoki, H. Sagayama, T. Moyoshi, A. Nakao, and T. Arima, Magnetic structure and phase transitions of A-site ordered double-Perovskite $SmBaMn_2O_6$, arXiv:2107.04179v2.

[34] S. Yamada, Y. Maeda, and T. Arima, Successive electronic transitions and anisotropic properties in a double-Perovskite $SmBaMn_2O_6$ single crystal, J. Phys. Soc. Jpn. **81**, 113711 (2012).

[35] J. B. Goodenough, Theory of the role of covalence in the Perovskite-type manganites [La, M(II)]MnO_3, Phys. Rev. **100**, 564 (1955).

[36] Z. Jirak, S. Krupica, Z. Simsa, M. Dlouha, and S. Vratislav, Neutron diffraction study of $Pr_{1-x}Ca_xMnO_3$, J. Magn. Magn. Mater. **53**, 153 (1985).

[37] T. Mizokawa and A. Fujimori, Spin, charge, and orbital ordering in Mn Perovskite oxides studied by model Hartree-Fock calculations, Phys. Rev. B **56**, R493(R) (1997).

[38] R. Maezono, S. Ishihara, and N. Nagaosa, Phase diagram of manganese oxides, Phys. Rev. B **58**, 11583 (1998).

[39] H. Kuwahara, T. Okuda, Y. Tomioka, A. Asamitsu, and Y. Tokura, Two-dimensional charge-transport and spin-vale effect in the layered antiferromagnet $Nd_{0.45}Sr_{0.55}MnO_3$, Phys. Rev. Lett. **82**, 4316 (1999).

[40] S. V. Streltsov, R. E. Ryltsev, and N. M. Chtchelkatchev, Ground-state structure, orbital ordering and metal-insulator transition in double-Perovskite $PrBaMn_2O_6$, J. Alloys Compd. **912**, 165150 (2022).

[41] D. Sekine, S. Yamada, and M. Matsubara, Direct detection of a polar order in a double Perovskite manganite $SmBaMn_2O_6$ using optical second harmonic generation, Meeting Abstract of the Physical Society of Japan 20pH1-1, (1214) (2025). (Japanese).

[42] K. Momma and F. Izumi, VESTA 3 for three-dimensional visualization of crystal, volumetric and morphology data, J. Appl. Crystallogr. **44**, 1272 (2011).